

## ARTICLE OPEN



# Vertical graphene on flexible substrate, overcoming limits of crack-based resistive strain sensors

Hong Ryeol Na<sup>1,5</sup>, Hyun Joo Lee<sup>2,5</sup>, Jae Ho Jeon<sup>1</sup>, Han-Jin Kim<sup>3</sup>, Sahng-Kyoon Jerng<sup>4</sup>, Sanjib Baran Roy<sup>1</sup>, Seung-Hyun Chun<sup>1</sup>✉, Sunghun Lee<sup>1</sup>✉ and Yong Ju Yun<sup>2</sup>✉

Resistive strain sensors (RSS) with ultrasensitivity have attracted much attention as multifunctional sensors. However, since most ultrasensitive RSS are designed by cracked conductive metals, the sensing performance is severely degraded due to accumulated structural deformation with consecutive cycles. To overcome such limitation, newly designed structures have been suggested, but the development of mechanosensors exhibiting superior stability and ultrasensitivity still remains a challenge. Here, we demonstrate that vertical graphene (VG) RSS with high sensitivity (gauge factor greater than 5000), remarkable durability (>10,000 cycles), and extraordinary resilience can serve multifunctional applications. We find that well-defined cracks on tufted network structure result in highly reversible resistance variation, especially revivable status even after broken current path, confirmed by microscopic in situ monitoring. The VG integrated with a wireless sensing system exhibits excellent timbre recognition performance. Our findings provide inspirable insights for mechanosensing system, making VG a promising component for future practicable flexible sensor technologies.

*npj Flexible Electronics* (2022)6:2; <https://doi.org/10.1038/s41528-022-00135-1>

## INTRODUCTION

From simple sensors to the Internet of Things (IoT), strain sensors have garnered attention for a myriad of fields, such as wearable devices, electronic skins, and human-machine interactive devices due to their high sensitivity and/or stretchability<sup>1–10</sup>. Flexible and stretchable electronics are being pursued to detect and monitor the cognitive status in individual's daily life as well as the subtle deformation of the objects<sup>11,12</sup>. A single resistive strain sensor (RSS) device usually combines the conductive metal and flexible substrate for outstanding electrical and mechanical properties<sup>3,11,13,14</sup>. Metals guaranteed excellent conductivity, resulting in high sensitivity, suffer from poor stretchability and durability owing to accumulated fatigue<sup>3,15,16</sup>, while organic nanocomposites, including graphene derivatives with excellent stretchability and durability, exhibit ultralow sensitivity (that is, low gauge factor (GF))<sup>5,7,9,17</sup>. For the hybrid application, diverse dimensional nanomaterials like nanotubes and nanoparticles have recently embedded in a strain sensor system<sup>18–21</sup>.

Capability to capture the physiological information and minute vibrations offers huge benefit for future bio-integrated electronics and robotic technologies, for which crack-based RSS have considered to be one of the representative candidates. Since cracks formed at metal thin film as a highly conducting channel break the pathway for current flow, tunneling current is dominated in transport mechanism, hence the resistance increases suddenly, i.e., large GF. The tunneling current is proportional to  $Hd \exp(-Hd)$ , where  $H$  is the tunneling barrier height dependent function, and  $d$  is the average tunneling distance<sup>22,23</sup>. Physiological and biometric signals such as human pulses, heartbeat rate, and laryngeal motion are relatively weak, thus crack-based RSS has been investigated to detect subtle and minute amplitudes. Moreover, owing to the electrical noise, it is imperative to develop an ultrasensitive RSS that can reliably detect even weak deformations<sup>14,24</sup>.

However, although crack-based RSS has shown paramount potential due to superior sensitivity and excellent electrical properties, undesirable mechanical properties such as accumulated fatigue and severe brittleness prevent an appropriate achievement for practical applications<sup>3,14–16,25</sup>, i.e., competitive trade-off among sensitivity, stretchability and durability. Since the cracks reconnect incompletely when the strain is concentrated and released, the durability and responded output signals are severely degraded on repeated cycles.

To maximize various functionalities and performance improvements, erstwhile RSS have been tested with the moderate strain range. When most mechanosensors have experienced the overload (that is, breakage of current path), their performance is significantly deteriorated or not restored<sup>3,14,26</sup>. Bio-inspired RSS reported by Kang et al. exhibited remarkable GF, but significant degradation of the sensitivity after consecutive cycles was shown, implying the problem in on-demand durability<sup>3</sup>. Recently protective polymer-coated layer and three-dimensional architectures were introduced to avoid mechanical deformation and fragmentation<sup>12,27–29</sup>. However, the convenient design for a single RSS consisting of conducting material and flexible substrate is still challenging as an aspect of cost-effectiveness. To be applicable in unpredicted extreme environment as well as in daily life, ultrasensitivity and extraordinary stability in a simple single device even after experiencing the overload should be simultaneously satisfied, leading us into the uncharted territory related on mechanosensors technology.

In this work, we introduce a highly durable and cyclable 3D vertical graphene (VG) on silicon elastomer polydimethylsiloxane (PDMS) structure with ultrasensitive mechanosensing properties (GF larger than 5,000), exhibiting minimal hysteresis when stretch and release. Surprisingly, approaching to the strain of 2.5%, the resistance showed infinity level in measurement range, while an

<sup>1</sup>Department of Physics and Astronomy, Sejong University, Seoul 05006, Korea. <sup>2</sup>Graduate School of Energy and Environment (KU-KIST Green School), Korea University, Seoul 02841, Korea. <sup>3</sup>Center for Energy Materials Research, Korea Institute of Science and Technology, Seoul 02792, Korea. <sup>4</sup>Graphene Research Institute, Sejong University, Seoul 05006, Korea. <sup>5</sup>These authors contributed equally: Hong Ryeol Na, Hyun Joo Lee. ✉email: schun@sejong.ac.kr; kshlee@sejong.ac.kr; yjyun0@korea.ac.kr

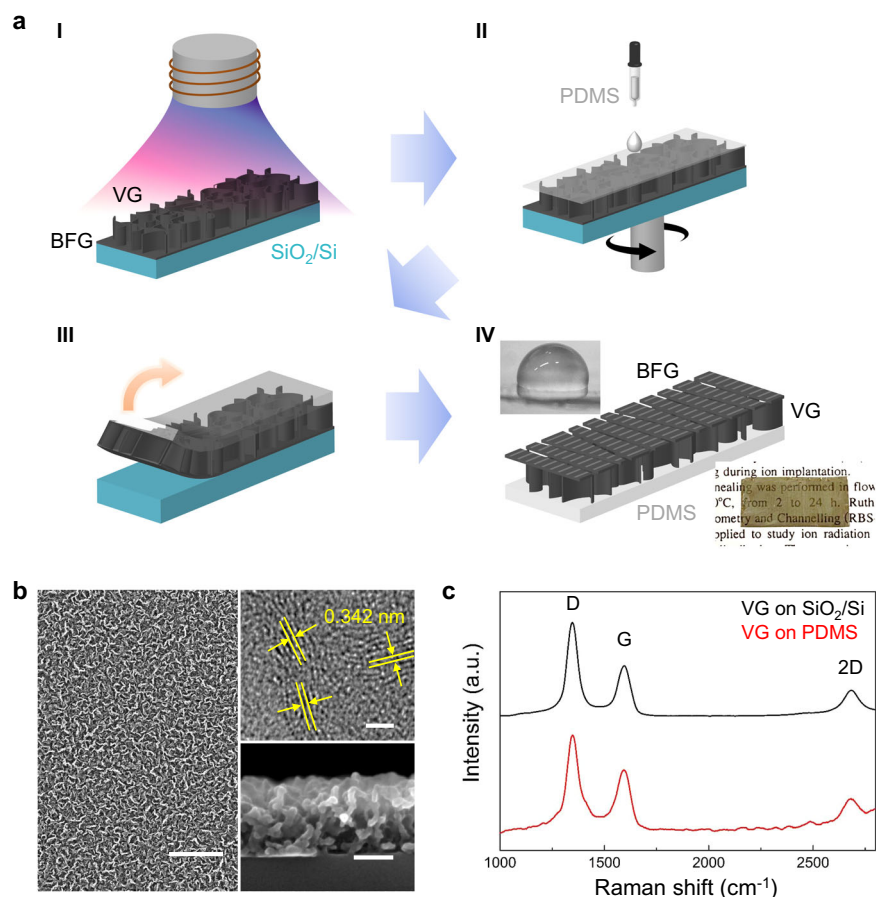


**Fig. 1 Fabrication of a VG on PDMS strain sensor and its characterization.** **a** Schematic illustration for the fabrication of a VG on PDMS strain sensor. A pristine VG film is directly grown on a  $\text{SiO}_2/\text{Si}$  substrate by PECVD (step I). A BFG layer is formed between the VG and  $\text{SiO}_2$  substrate during the initial VG growth. A dilute PDMS mixture (10:1) is drop cast onto the VG film, followed by spin-coating (step II). The PDMS film is degassed using a vacuum desiccator and cured for 2 h at 70 °C. After curing, PDMS/VG is mechanically peeled off the  $\text{SiO}_2$  substrate (step III). When flipped over, the final product, BFG/VG on PDMS is obtained (step IV). Insets of step IV: contact angle optical image of a water droplet on VG (upper left) and photograph (lower right) of VG on PDMS after removal from the  $\text{SiO}_2$  substrate. **b** SEM image of an as-grown VG films on a  $\text{SiO}_2$  substrate. Scale bar, 3  $\mu\text{m}$ . The top inset shows an HR-TEM image of a VG films, confirming the interplanar spacing of 0.342 Å, comparable to that of graphite. Scale bar, 2 nm. The bottom inset shows a cross-sectional view of a VG films on  $\text{SiO}_2$ , revealing a tufted 3D network structure. Scale bar, 100 nm. **c** Raman spectra of VG on  $\text{SiO}_2/\text{Si}$  and PDMS. The clear peaks at around 1350  $\text{cm}^{-1}$  (D peak), 1585  $\text{cm}^{-1}$  (G peak), and 2690  $\text{cm}^{-1}$  (2D peak) are observed for both samples.

almost perfectly restored resistance level compared to the pre-stretched resistance was observed when released again, indicating revivable status of VG RSS. Over 100-fold resistance change was repeated more than 10,000 cycles to demonstrate the high durability and stability without downward drift. In situ microscopic monitoring revealed mechanical dynamics of cracks formed on a unique 3D VG network structure. Finally, we demonstrated potential applications by using VG RSS integrated with a wireless sensing system, showing systematic alarm indicator and excellent timbre/phonation recognition performance.

## RESULTS AND DISCUSSION

### Fabrication of VG on PDMS strain sensors

We synthesized VG on a  $\text{SiO}_2/\text{Si}$  wafer by using the plasma-enhanced chemical vapor deposition (PECVD) method (I in Fig. 1a and Supplementary Note 1). As seen in Fig. 1b, the morphology of the as-synthesized VG shows tufted graphene networks comprising 10–35 layers, as revealed by the transmission electron microscopy (TEM) image (upper right of Fig. 1b). Note that a buffer flat graphene (BFG) layer with 2–4 nm thick was formed between the VG and  $\text{SiO}_2$  wafer during the initial VG growth (Supplementary Fig. 1). The height of the petal-shaped VG was

approximately 200 nm (lower right of Fig. 1b), and the root-mean-square roughness of the surface was measured to be 17.5 nm by atomic force microscopy (AFM), indicating high density of the VG sheets (Supplementary Fig. 2). Elastomeric liquid PDMS was then cast and cured on the as-synthesized VG (II in Fig. 1a), and the composite was manually peeled off from the  $\text{SiO}_2$  substrate (III in Fig. 1a). Casting at speeds above 1000 rpm resulted in a film that rolled upon itself after manual peeling (Supplementary Fig. 3). The unavoidable cracks between the VG and  $\text{SiO}_2$  wafer were formed regardless of spin rate due to the manual peeling process (Supplementary Note 2 and Supplementary Fig. 4), affecting the mechanical sensing performance, which will be discussed later. Flipping the film over yielded the final VG strain sensor (VGS), with a top-to-bottom sequence of BFG/VG/PDMS (IV in Fig. 1a).

The VGS showed moderate transmittance and hydrophobicity (upper left and lower right of IV in Fig. 1a and Supplementary Fig. 5), suggesting its feasibility as an electronic skin sensor<sup>11</sup>. We compared the resistance of multiple samples, revealing a 5~10-fold increase in the resistance from the samples on  $\text{SiO}_2/\text{Si}$  without PDMS to the delaminated VGSs with PDMS (Supplementary Fig. 6). The Raman spectra, however, showed the same graphitic D and G band features in both samples (Fig. 1c), confirming the graphene characteristics<sup>30</sup>.

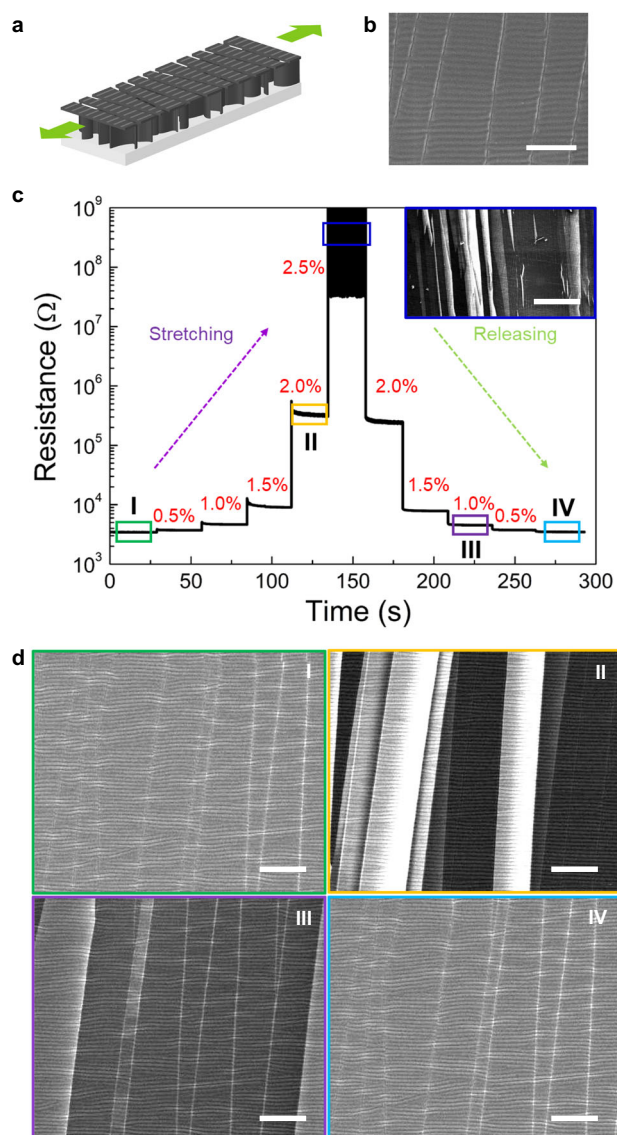


**Fig. 2 Restorable and stable VGS-V behavior.** **a** Illustration of VGS when the elongated direction is perpendicular to the cracks on the BFG. **b** Enlarged SEM image of surface on BFG, clearly showing well-aligned cracks on the BFG. Scale bar, 50  $\mu\text{m}$ . **c** Resistance as a function of time with applied stepwise strain. Approaching 2.5% strain, the resistance reaches in unmeasurable range, namely, the current path is broken, which the corresponded in situ SEM image is shown in the inset (Scale bar, 500  $\mu\text{m}$ ). However, the resistance is restored after the strain is released, and the post-overloaded resistance is almost the same to the pre-overloaded resistance at each strain. **d** In situ SEM images of VGS during stretching (I (0%), green box and II (2%), yellow box)/releasing (III (1%), purple box and IV (0%), blue box), which are corresponded to those boxes in (c). Scale bar, 200  $\mu\text{m}$ .

### Mechanical and electronic dynamics of VGS during stretching and releasing

The electrical resistance of VGSs under strain was evaluated with a home-built tensile measurement system (see Methods). The cracks formed on the BFG were very uniformly aligned in one direction as shown in Fig. 2b, unlike the randomized cracks' direction in previous VGS reports<sup>29,31–33</sup>. Also, wrinkled crests were formed perpendicular to and between the cracks on the BFG because of Poisson's effect (Fig. 2b)<sup>34</sup>. When the VGS was elongated perpendicular to the crack direction on the BFG (Fig. 2a), the

resistance abruptly increased with stepwise increasing strain, then finally the resistance reached in unmeasurable range (overload) at a strain of 2.5%, as shown in Fig. 2c. Surprisingly, upon the VGS released, the resistance was restored to the same level before the VGS was stretched, i.e., no hysteresis was observed, indicating completely reversible behavior under strain and the reliability of the strain sensors<sup>5</sup>.

What we are emphasizing in this work is that the resistance is perfectly restored again, even after the current does not flow any more, namely the breakage of the current path. To the best of our knowledge, the sensing performance before and after the overload in resistance level is the first demonstration in a simple single strain sensor without additional structures. To investigate the origin of revivable behavior in detail, we carried out in-depth microscopic measurement including in situ scanning electron microscopy (SEM) monitoring for the mechanical dynamics of VGS structure.

At 0% strain, despite the appearance of cracks on the BFG, charge transport occurred through the tufted 3D VG network and the top BFG surface (I, green box in Fig. 2c, d). Increasing the strain began fragmentation of the top BFG surface on 3D VG network, then the resistance significantly increased with enfeebled fastening between 3D VG network (II, yellow box in Fig. 2c, d). Finally, the 3D VG network fully disconnected at a large strain and the PDMS layer was torn (Supplementary Fig. 8). Surprisingly, however, when released and returning to 0% strain, the disconnected and torn VGS re-adhered, and a new VG network was reconstructed by the Velcro-like 3D network, perfectly restoring the initial resistance (III and IV, purple and blue box in Fig. 2c, d and Supplementary Movie 1). We performed same measurement using several samples for reproducible revival features, exhibiting perfect restoration of the resistance after the breakage of the current path.

A GF is one of the important key factors considered as sensing performance, which is commonly used to evaluate the strain sensitivity in resistive strain sensors. In general, GF is defined by the formula;  $GF = (R - R_0)/(R_0\epsilon)$ , where  $R_0$  is the resistance at 0% strain and  $\epsilon$  is the applied strain. Figure. 3a shows the GF at specific strains during stretching and releasing. At a strain of 2%, the GF remarkably exceeded 5,000. We summarize the performance of state-of-the-art resistive strain sensors in Table 1. Although the GFs in Table 1 only reveal the estimated values at 2% for meticulous comparison, the strain sensitivity in our VGS is outstanding compared to the other strain sensors. Most strikingly, the GF of our VGS that has been restored even after severe damage is almost no difference from the initial value before the breakage, as shown in Figure. 3a. To date, the studies for the structural and electrical behaviors after the overloaded strain, reaching severe damage of the sensors, are rare in crack-based resistive strain sensors.

Highly consistent and reliable resistance variation before and after overload, where the resistance has been in unmeasurable range, makes VGS a feasible mechanosensing platform to develop the future sensory technology and expand the potential application in extreme environments. Fig. 3b demonstrates the ability of VGS to withstand 10,000 consecutive stretching-releasing cycles between 0 and 2% strain. The electrical responses showed almost no degradation, indicating excellent long-term durability of VGS. Retaining steady resistance holding high GF (>5000) without a significant downward drift is a core concern for competitive strain sensor application. Note that unlike other RSS reports that tested the stability with moderate strain, highly stable status exhibiting large resistance variation over 100-fold change under the consecutive cycle is highlighted in our work. The response and recovery times of the VGS were approximately 200 and 100 ms without latency, respectively. The parameters to reflect the performance were summarized with recent reports in Table 1.

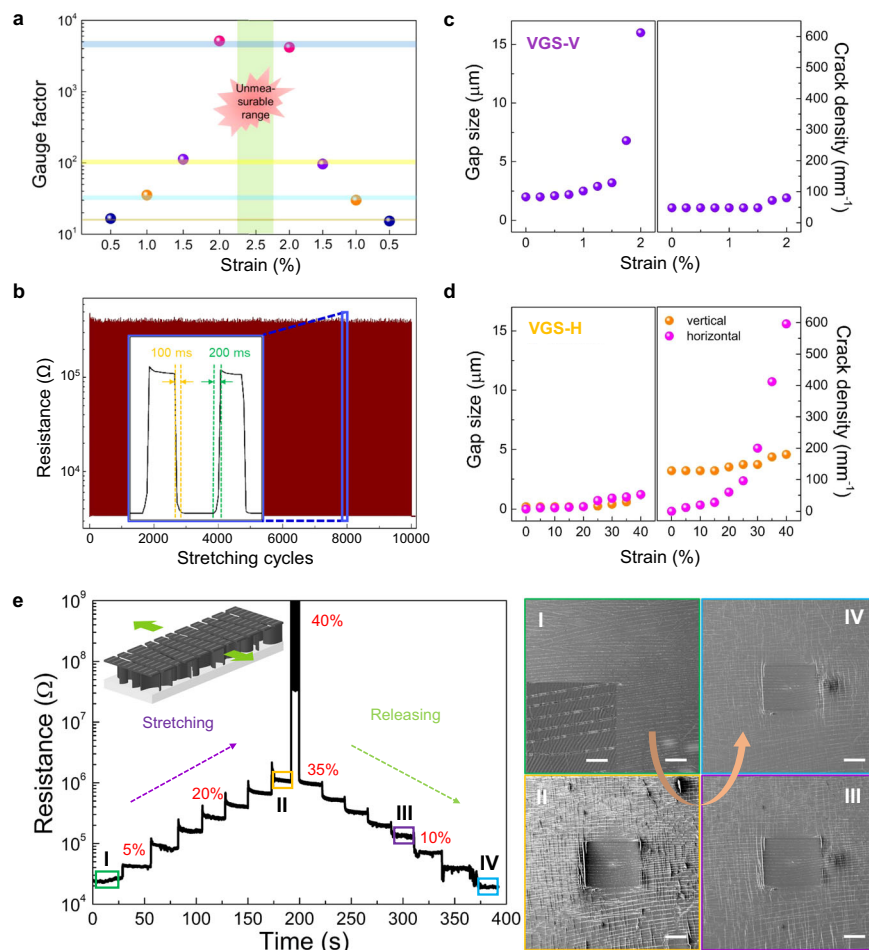


**Fig. 3 VGS performance and sensing mechanism.** **a** Gauge factor as a function of strain, estimated from Fig. 2c. Except for 2% strain, no noticeable changes at each strain are observed, indicating highly reversible behavior. The width of highlighted color bars indicates the difference between averaged gauge factors when stretching and releasing at specific strains. **b** Resistance measured between 0 and 2% strain for 10,000 consecutive cycles with a strain sweep rate of 1 mm/s and 0.1 s hold time at the peak. The response and recovery times are approximately 200 and 100 ms from the enlarged curves in blue box. **c, d** Gap size between cracks and crack density versus applied strain for VGS-V (**c**) and VGS-H (**d**). In **e** the 'vertical' cracks are those formed initially during removal from the  $\text{SiO}_2$  substrate and the 'horizontal' cracks are those newly formed during stretching. **e** Resistance as a function of time with applied stepwise strain when the elongated direction is parallel to the cracks on the BFG (upper illustration). The resistance approaches infinity when the applied strain reaches up to 40%, namely, the current path is broken. But, the resistance recovers to the initial value during release, and the post-overload resistance is almost the same to the pre-overload resistance at each strain. Right panel of **e** In situ SEM images of VGS-H during stretching (I (0%), green box and II (35%), yellow box)/release (III (15%), purple box and IV (0%), blue box). Scale bars, 200  $\mu\text{m}$ . Inset in I, enlarged SEM image, clearly showing vertical cracks on the BFG. Scale bar, 50  $\mu\text{m}$ .

The thickness of conducting materials affects their structural deformation, and a thinner layer is more beneficial for strain sensors due to the stiffness and density<sup>3,27</sup>. Contrary to the previous VGS<sup>29,31–33</sup>, whose thickness was 1–4  $\mu\text{m}$ , our 200 nm thick VGS showed an initial gap of  $\sim 2 \mu\text{m}$  even when unstrained (Supplementary Fig. 4). In thick 3D dilational structures, when the tensile or compressive forces are applied, the dispersive forces toward in-plane direction increase, leading to negative Poisson's ratio<sup>34–36</sup>. In this case, including the previous VGS reports<sup>29,31–33</sup>, the direction of unavoidable cracks on BFG between VG and basal plane is random rather than aligned. Since the VG used in our experiments has 200 nm thickness and highly tufted density confirmed by AFM, it is assumed to be a rigid structure possessing a positive Poisson's ratio. Thus, during manual peeling process, the cracks on BFG generated by tensile force are well aligned in one direction, and the wrinkled wavy crests are formed between cracks, as shown in Fig. 2b. Such unique structural feature makes our VGS an ultrasensitive and permanent strain sensor, superior to crack-based strain sensors comprising highly

conductive metal<sup>3,15,16</sup>. Fig. 3c displays the size of the gap between the cracks and the crack density of VGS as a function of strain. The crack density was almost constant, while the gap size changed dramatically with increasing strain, thus blocking the current path. No newly created cracks were observed with increasing elongation, resulting in perfectly restored GF after breakage of current path, i.e., disconnection-reconnection process undergone by Velcro-like 3D network.

To further investigate the relation with initial cracks and elongation direction, we performed the same experiment except with the VGS elongation parallel to the crack (VGS-H), as seen in the inset of Fig. 3e. Compared to their values for elongating the VGS-V (perpendicular to the crack direction), the maximum strain to reach overload and the time to stabilize the saturated resistance increased, giving rise to lower GF ( $\sim 34.7$ ) and durability (Supplementary Fig. 9). However, the resistances at each strain in VGS-H after breakage of the current path returned to nearly the same levels as before overload, as same as the VGS-V. Interestingly, at over 35% strain, very large stringy cracks newly formed

**Table 1.** Summary of performance comparison for state-of-the-art strain sensors.

Materials	Estimated GF at 2%	Durable cycles (GF when tested)	Downward drift (%)	Refs.
Pt on PUA <sup>a</sup>	2079	5000 (900)	37	3
CFPC <sup>b</sup> /TPU <sup>c</sup>	9400	1000 (923)	12	10
BP <sup>d</sup> /LEG <sup>e</sup> on SEBS <sup>f</sup>	81.2	18,400 (60)	58.3	12
Au on PDMS	3500	1000 (40)	12.5	15
SBR/NR-GE <sup>g</sup>	<50	300 (27)	12.5	17
Graphene/carbon black/Ni sponge	36	1200 (133)	6.3	28
Sandwich-structured VG/PDMS	~910	1000 (25)	15	29
UP-VG/PDMS <sup>h</sup>	72	1000 (87.5)	20	32
CNT/PDMS	1	10,000 (8)	~8	40
VG on PDMS	5,200	10,000 (5200)	10	This work

<sup>a</sup>Polyurethane acrylate; <sup>b</sup>Carbon fiber polymer composites; <sup>c</sup>thermoplastic polyurethane; <sup>d</sup>Black phosphorus; <sup>e</sup>Laser-engraved graphene; <sup>f</sup>Polystyrene-*block*-poly(ethylene-*ran*-butylene)-*block*-polystyrene; <sup>g</sup>Styrene rubber/natural rubber-functionalized graphene; <sup>h</sup>Ultrasonic peeling method.

perpendicular to the initial cracks, as confirmed by in situ SEM measurements (yellow box in Fig. 3e, marked as II). Wrinkled crests emerged between the initial cracks when the cracks on top surface were compressed in the transverse direction, which could play a significant role in the different sensitivities of the VGS depending on the elongation direction. Since the stringy cracks in VGS-H occurred along the wrinkles, the current channel participating in charge transport can be retained at greater strains in VGS-H than in VGS-V. Figure. 3d displays the size of the gaps between the cracks and the crack density for VGS-H, where vertical (initial cracks) and horizontal cracks (newly formed cracks) are divided for convenience. Unlike crack distribution in VGS-V, the gap size increased only slightly, but the density of newly created cracks perpendicular to the initial cracks (marked as horizontal, magenta circles) increased exponentially at high strain, impeding the charge transport.

### Applications of wireless VGS module

To further demonstrate the restoration of the initial resistance during strain cycling and the feasible capabilities, we tested light-emitting diodes (LEDs) in series as a graded alarm switch during stretching/releasing (Fig. 4a and Supplementary Movie 2). As shown in Fig. 4a, since the electrical resistance is modified by the applied strain, the strain values can be quantified as the number of lit LEDs in a programmed circuit. Once exceeding a critical strain, all LEDs were turned off, implying suitable applications for an alarm signal indicator in an intelligent visual-control system.

Another application for our stretchable VGS is real-time continuous monitoring, which requires high sensitivity and superior stability such as our VGS exhibits. To validate its capability to detect subtle mechanical forces, such as mechanical vibrations of skin or acoustic vibrations of an audio system, we explored several applications. Furthermore, to expand the VGS potential applications to wearable strain sensors, especially in wireless sensing systems, the ability of a module composed of the VGS, a microcontroller, a Bluetooth transmitter and a lithium-ion battery was investigated (Fig. 4b). Firstly, the VGS was utilized as a wearable RSS conformally attached on the phalangeal joint of the index finger by using ultrathin and transparent medical tape (Tegaderm<sup>TM</sup> Film 1622W, 3M), where recorded the bending/stretching motion of a finger in real time (Fig. 4c, d and Supplementary Movie 3). The resistance changes induced by the mechanical motion of the finger were clearly exhibited, and the initial jump in resistance increased with the bending angle.

As the potential of using the VGS for large motions was demonstrated, we moved to test its potential for timbre recognition. As a pivotal component in future IoT technology,

timbre recognition has been an integral part of strain sensors<sup>37</sup>. Since the vibration produced by an audible wave is fairly weak, ultrasensitivity is essential for a sound detector that can monitor diverse and sophisticated vibrations. We measured the time-dependent resistance variation of a VGS module attached to the surface of a vibrating loudspeaker membrane that was playing classical music (Beethoven Symphony No. 5, 'Fate': Allegro con brio). The  $\Delta R/R_0$  peak patterns showed similar shapes to the acoustic waveform from the loudspeaker (Fig. 4e), confirming the capability for timbre recognition. We also examined physiological laryngeal motion by using VGS module attached onto a tester's throat (Fig. 4f). Medical tape was attached over the VGS edge, and wires connected the VGS with an interface circuit. Figure. 4g shows the  $\Delta R/R_0$  response to changes in laryngeal prominence during speech in two different languages, English and Korean. Although several words in the two languages with the same meanings, such as 'A', 'B', and 'hello graphene' in English and '가 (ga)', '나 (na)', and '안녕 그래핀 (annyeong geulaepin)' in Korean, were repeated, similar patterns with repeatable same phonation were detected for each example in each language. Of particular interest in our timbre recognition system is the amplitude of the  $\Delta R/R_0$ . Most of the  $\Delta R/R_0$  values displayed in Fig. 4e and g indicated an increase of 100% over the initial resistance, significantly better than the limited sensitivity shown in previous reports<sup>3,32,38–40</sup>. Our VGS system may be promising in technologies such as a device for phonation rehabilitation exercises and a physiological monitor for the early detection of sudden infant death syndrome (SIDS) in sleeping infants<sup>41,42</sup>.

In summary, we fabricated an ultrasensitive VGS that exhibited highly reversible and restorable behavior under strain, even after broken current path, which was confirmed by in situ SEM measurements and relative resistance variations. The crack-based VGS showed the incredible performance as compared with recent crack-based RSS (Supplementary Table 1). The dependence of the sensing performance on the elongation direction with regard to the initial cracks indicates that our VG mechanosensing system has multiple performance ranges. The marriage of extraordinary sensing performance and wireless timbre recognition shown here provides great flexibility in meeting the demands for the platform to develop future IoT technologies.

## METHODS

### Growth of VG

Pristine VG films were directly grown on 4-inch SiO<sub>2</sub>/Si substrate using a PECVD. The inductively coupled plasma CVD technique enabled large-scale VG film growth at relatively low temperature<sup>29,31–33</sup>. The VG films were grown at 770 °C for 1 h with a mixture gas of CH<sub>4</sub> and H<sub>2</sub> (10 standard

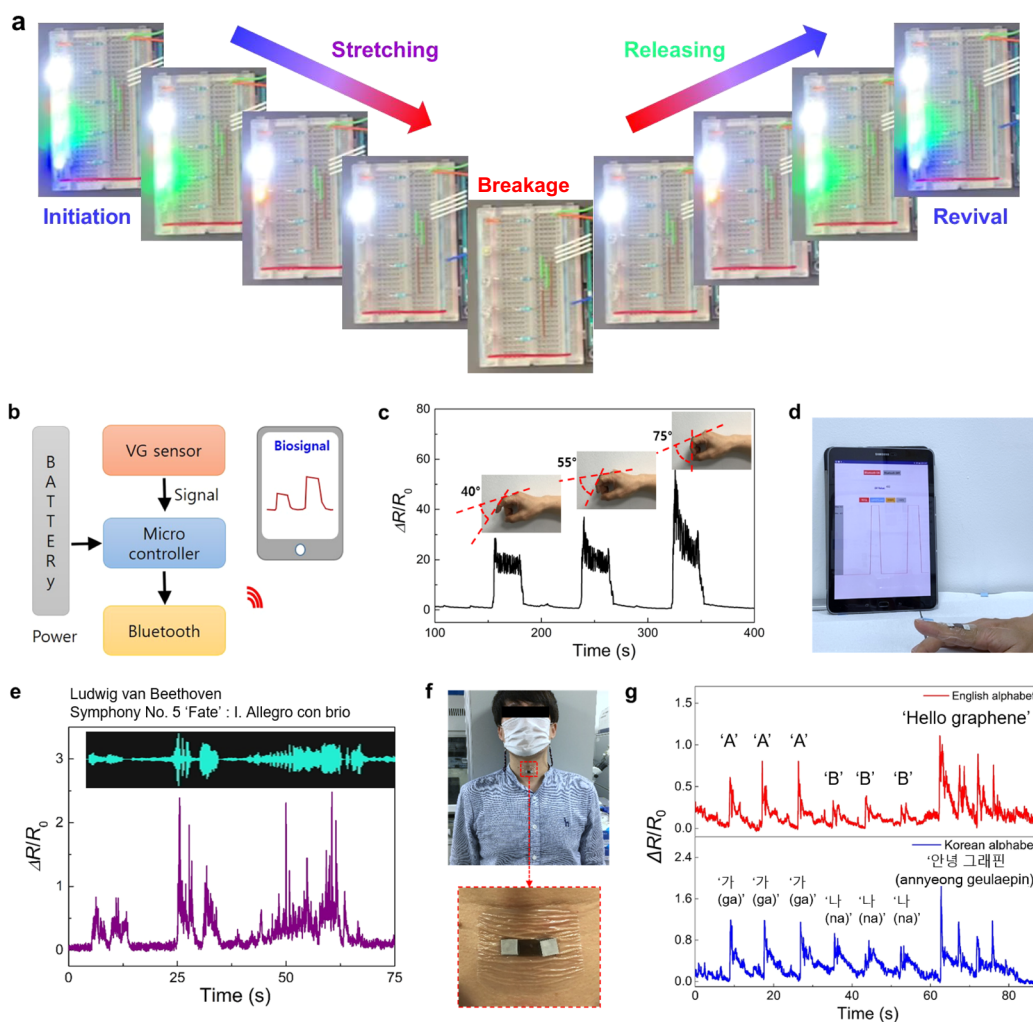


**Fig. 4 Various applications of VGs.** **a** Snapshots of four LEDs that indicate the resistance level from low resistance (all lit) to overload (all off). A series of blinking LEDs operates stably even after the breakage status. **b** Operational block diagram for the wearable system operation. **c** Relative resistance variation for VGs under different bending angles. Insets show the bending angles of the index finger. **d** Image of the wearable system integrated with strain sensor for real-time finger bending monitoring. A Bluetooth transmitter sends sensor measurements for real-time data readout and logging on a tablet. **e** Relative resistance variation of VGs attached to a loudspeaker playing classical music (Ludwig van Beethoven Symphony No.5 in C minor, Op. 67 'Fate': Allegro con brio). **f** Photograph of a wireless VGs conformally attached onto a tester's throat for the relative resistance variation during speech involving different languages and words, 'A', 'B', and 'hello graphene' in English, and '가 (ga)', '나 (na)', and '안녕 그래핀 (annyeong geulaepin)' (with the same meaning) in Korean are repeated. All of the signals are recorded clearly and exhibit distinguishable phonation.

cubic centimeters per min (sccm) each), generating a plasma at a radio frequency (RF) power of 50 W under a 10 mTorr total chamber pressure. The structure and formation of VG were confirmed by FE-SEM and HR-TEM measurements, and chemical characteristics were analyzed by Raman and XPS spectroscopy<sup>43</sup>.

#### Fabrication and characterization of VG on PDMS

As-grown VG films on SiO<sub>2</sub>/Si substrate were cut into 1 × 3 cm<sup>2</sup> pieces for strain measurements before introducing PDMS. A commercial PDMS kit (Sylgard 184 silicone elastomer kit, Dow Corning) was used to prepare a supporting elastic layer. A silicone elastomer base and curing agent mixture (10:1 weight ratio of prepolymer to crosslinker) was coated on VG films by conventional spin-coating at 1000 rpm, degassed using a vacuum desiccator for 2 h, and cured at 70 °C for 2 h on a hotplate. All PDMS/VG samples were mechanically peeled off the SiO<sub>2</sub>/Si substrates.

To determine the hydrophobicity, the contact angle ( $\theta_c$ ) was measured at room temperature after dropping 10  $\mu$ L of Milli-Q water on the VG on PDMS using a micropipette. The angle between the VG films on the PDMS surface and water droplet was determined by using the Image-J program for pictures photographed with an iPhone. To confirm the graphene nature of the materials, Raman spectra of VG films both on SiO<sub>2</sub>/Si

substrates and after removal were obtained by a Raman spectroscopy system (inVia confocal Raman microscope, Renishaw), using a 514.5 nm of a sapphire laser (Sapphire 514 FP, Coherent) excitation source operated at 2 mW. The laser beam was focused onto the VG by a ×50 microscope objective lens (Leica Microsystems GmbH).

#### Measurements of resistance under strain

Stretchable VG films 3.0 cm long and 1.0 cm wide were placed in a computer-controlled, motorized actuating system for repeated stretching-releasing tests. One end of each sample was attached to a fixed stage, and the other end was attached to a movable stage. The electrical resistance was measured using a digital multimeter (34461A, Keysight Technologies) using a two-probe method in a controlled temperature and humidity atmosphere (20 ± 1 °C and 50 ± 10% relative humidity). Stability tests with up to 10,000 cycles were performed with a movement rate of 1.0 mm/s under various strains from 0 to 2% for VGs-V and from 0 to 30% for VGs-H.

For a light-indicating the resistance levels from low resistance to overload of the VGs, we used Arduino UNO programed by C++ code, which is compact and easy to connect another measurement system. While applying 5 V to the VG and 1 M $\Omega$  reference resistor in series, LEDs on

the circuit turn on normally. Then, specific colored LEDs were turned off one by one when resistance values reached the following conditions;  $R \geq 10^4 \Omega$  (blue),  $\geq 10^6 \Omega$  (green),  $\geq 10^7 \Omega$  (orange), and  $\geq 10^9 \Omega$  (white).

### In situ SEM measurements

In situ SEM tension and compression tests were carried out using a microtensile tester (GatanMicroTest300N) installed in an SEM system (Inspect F, FEI) under a cross-head speed of 1.5 mm/min. SEM images were taken in real-time to produce video files. Deformation was intermittently halted for approximately one minute at different predetermined strain levels to capture high-quality images.

### Wearable system for wirelessly mechanical forces monitoring

We fabricated a wearable monitoring system that used VGS-V for index finger motion monitoring, a microprocessor (8-bit microcontroller ATmega328P chip) for data processing, a Bluetooth module (2.4 GHz Bluetooth CC2540 chip with sensitivity of  $-93$  dBm) for wireless data transmission, and a rechargeable lithium-ion battery (3.7 V, 150 mAh) as a power supply. The wearable system was wirelessly connected to a tablet (Samsung Galaxy S3). User interface code for mechanical force monitoring were created with App Inventor II (open source software program).

### DATA AVAILABILITY

The data that support the findings of this study are available from the corresponding author upon reasonable request.

Received: 20 July 2021; Accepted: 17 December 2021;

Published online: 26 January 2022

### REFERENCES

- Pang, C. et al. A flexible and highly sensitive strain-gauge sensor using reversible interlocking of nanofibers. *Nat. Mater.* **11**, 795–801 (2012).
- Jeong, J.-W. et al. Materials and optimized designs for human-machine interfaces via epidermal electronics. *Adv. Mater.* **25**, 6839–6846 (2013).
- Kang, D. et al. Ultrasensitive mechanical crack-based sensor inspired by the spider sensory system. *Nature* **516**, 222–226 (2014).
- Kim, J. et al. Stretchable silicon nanoribbon electronics for skin prosthesis. *Nat. Commun.* **5**, 5747 (2014).
- Amjadi, M., Kyung, K.-U., Park, I. & Sitti, M. Stretchable, skin-mountable, and wearable strain sensors and their potential applications: a review. *Adv. Funct. Mater.* **26**, 1678–1698 (2016).
- Ge, J. et al. A stretchable electronic fabric artificial skin with pressure-, lateral strain-, and flexion-sensitive properties. *Adv. Mater.* **28**, 722–728 (2016).
- Shi, G. et al. Highly sensitive, wearable, durable strain sensors and stretchable conductors using graphene/silicon rubber composites. *Adv. Funct. Mater.* **26**, 7614–7625 (2016).
- Miyamoto, A. et al. Inflammation-free, gas-permeable, lightweight, stretchable on-skin electronics with nanomeshes. *Nat. Nanotechnol.* **12**, 907–913 (2017).
- Heikenfeld, J. et al. Wearable sensors: modalities, challenges, and prospects. *Lab Chip* **18**, 217–248 (2018).
- Araromi, O. A. et al. Ultra-sensitive and resilient compliant strain gauges for soft machines. *Nature* **587**, 219–224 (2020).
- Liu, H. et al. Electrically conductive polymer composites for smart flexible strain sensors: a critical review. *J. Mater. Chem. C* **6**, 12121–12141 (2018).
- Chhetry, A. et al. Black phosphorus@laser-engraved graphene heterostructure-based temperature-strain hybridized sensor for electronic-skin applications. *Adv. Funct. Mater.* **31**, 2007661 (2021).
- Liao, X. et al. Ultrasensitive and stretchable resistive strain sensors designed for wearable electronics. *Mater. Horiz.* **4**, 502–510 (2017).
- Park, B. et al. Dramatically enhanced mechanosensitivity and signal-to-noise ratio of nanoscale crack-based sensors: effect of crack depth. *Adv. Mater.* **28**, 8130–8137 (2016).
- Yang, T. et al. Structural engineering of gold thin films with channel cracks for ultrasensitive strain sensing. *Mater. Horiz.* **3**, 248–255 (2016).
- Han, Z. et al. High-performance flexible strain sensor with bio-inspired crack arrays. *Nanoscale* **10**, 15178–15186 (2018).
- Lin, Y. et al. A highly stretchable and sensitive strain sensor based on graphene-elastomer composites with a novel double-interconnected network. *J. Mater. Chem. C* **4**, 6345–6352 (2016).

- Shi, J. et al. Graphene reinforced carbon nanotube networks for wearable strain sensors. *Adv. Funct. Mater.* **26**, 2078–2084 (2016).
- Kim, K., Lee, J., Jo, E., Sim, S. & Kim, J. Patterned carbon nanotube bundles as stretchable strain sensors for human motion detection. *ACS Appl. Nano Mater.* **3**, 11408–11415 (2020).
- Shengbo, S. et al. Highly sensitive wearable strain sensor based on silver nanowires and nanoparticles. *Nanotechnology* **29**, 255202 (2018).
- Jheng, W.-W. et al. Gold nanoparticle thin film-based strain sensors for monitoring human pulse. *ACS Appl. Nano Mater.* **4**, 1712–1718 (2021).
- Lu, J. R. et al. Piezoresistive materials from directed shear-induced assembly of graphite nanosheets in polyethylene. *Adv. Funct. Mater.* **15**, 1358–1363 (2015).
- Zhao, J. et al. Tunable piezoresistivity of nanographene films for strain sensing. *ACS Nano* **9**, 1622–1629 (2015).
- Lee, H. S. et al. Flexible inorganic piezoelectric acoustic nanosensors for biometric artificial hair cells. *Adv. Funct. Mater.* **24**, 6914–6921 (2014).
- Kim, D.-S. et al. Highly durable crack sensor integrated with silicone rubber cantilever for measuring cardiac contractility. *Nat. Commun.* **11**, 535 (2020).
- Park, B. et al. A semi-permanent and durable nanoscale-crack-based sensor by on-demand healing. *Nanoscale* **10**, 4354–4360 (2018).
- Wang, X. et al. Self-cross-linked arrays enabled flexible mechanical sensors for monitoring the body tremor. *npj Flex. Electron.* **4**, 8 (2020).
- Sun, S. et al. A wearable, waterproof, and highly sensitive strain sensor based on three-dimensional graphene/carbon black/Ni sponge for wirelessly monitoring human motions. *J. Mater. Chem. C* **8**, 2074–2085 (2020).
- Wu, S., Peng, S., Han, Z. J., Zhu, H. & Wang, C. H. Ultrasensitive and stretchable strain sensors based on maze-like vertical graphene network. *ACS Appl. Mater. Interfaces* **10**, 36312–36322 (2018).
- Malard, L. M., Pimenta, M. A., Dresselhaus, G. & Dresselhaus, M. S. Raman spectroscopy in graphene. *Phys. Rep.* **473**, 51–87 (2009).
- Huang, S. et al. Stretchable strain vector sensor based on parallelly aligned vertical graphene. *ACS Appl. Mater. Interfaces* **11**, 1294–1302 (2019).
- Deng, C. et al. Ultrasensitive and highly stretchable multifunctional strain sensors with timbre-recognition ability based vertical graphene. *Adv. Funct. Mater.* **29**, 1907151 (2019).
- Deng, C. et al. High-performance capacitive strain sensors with highly stretchable vertical graphene electrodes. *J. Mater. Chem. C* **8**, 5541–5546 (2020).
- Wang, Y. et al. Giant Poisson's effect for wrinkle-free stretchable transparent electrodes. *Adv. Mater.* **31**, 1902955 (2019).
- Bückmann, T. et al. On three-dimensional dilational elastic metamaterials. *New J. Phys.* **16**, 033032 (2014).
- Carta, G., Brun, M. & Baldi, A. Design of a porous material with isotropic negative Poisson's ratio. *Mech. Mater.* **97**, 67–75 (2016).
- Zhu, M. et al. Tactile and temperature sensors based on organic transistors: towards e-skin fabrication. *Front. Phys.* **16**, 13302 (2021).
- Wang, Y. et al. Ultra-sensitive graphene strain sensor for sound signal acquisition and recognition. *Nano Res.* **8**, 1627–1636 (2015).
- Fang, X., Tan, J., Gao, Y., Lu, Y. & Xuan, F. High-performance wearable strain sensors based on fragmented carbonized melamine sponges for human motion detection. *Nanoscale* **9**, 17948–17956 (2017).
- Gao, Y. et al. highly sensitive strain sensors based on fragmented carbon nanotube/polydimethylsiloxane composites. *Nanotechnology* **29**, 235501 (2018).
- Conroy, E. R. et al. Effect of variations to a simulated system of straw phonation therapy on aerodynamic parameters using excised canine larynges. *J. Voice* **28**, 1–6 (2014).
- Fleming, P. J. et al. Interaction between bedding and sleeping position in the sudden infant death syndrome: a population based case-control study. *Br. Med. J.* **301**, 85–89 (1990).
- Akbar, K. et al. Superaerophobic graphene nano-hills for direct hydrazine fuel cells. *NPG Asia Mater.* **9**, e378 (2017).

### ACKNOWLEDGEMENTS

The authors thank H.-J. Kim for the transmittance measurements of VG on PDMS. Also the authors thank M.-H. Kim, M.S. Hyun and Y.C. Park for SEM measurement and useful discussion. S.-H.C. acknowledges the support from the National Research Foundation of Korea (NRF) grant funded by the Korean government (No. 2016R1E1A1A01942649). S.L. acknowledges the support from the National Research Foundation of Korea (NRF) grant funded by the Korean government (2018R1D1A1B07048109 and 2021R1F1A1050726). Y.J.Y. acknowledges the support from the National Research Foundation of Korea (NRF) grant funded by the Korean government (grant nos. 2018R1D1A1B07045581) and from a Korea University Grant.

## AUTHOR CONTRIBUTIONS

H.R.N. and H.J.L. contributed equally to this work. S.-H.C., S.L., and Y.J.Y. conceptualized the project and designed the experiments. S.-K.J. and S.B.R. grew the VG samples. H.R.N., J.H.J., and S.L. fabricated VG on PDMS and characterized the samples. H.J.L. and Y.J.Y. carried out all experiments for stretchable sensor characterization, data collection, and data analysis. H.J.K. contributed to in situ SEM measurement. H.J.L., S.-H.C., S.L., and Y.J.Y. co-wrote the manuscript. All authors discussed the results and provided feedback.

## COMPETING INTERESTS

The authors declare no competing interests.

## ADDITIONAL INFORMATION

**Supplementary information** The online version contains supplementary material available at <https://doi.org/10.1038/s41528-022-00135-1>.

**Correspondence** and requests for materials should be addressed to Seung-Hyun Chun, Sunghun Lee or Yong Ju Yun.

**Reprints and permission information** is available at <http://www.nature.com/reprints>

**Publisher's note** Springer Nature remains neutral with regard to jurisdictional claims in published maps and institutional affiliations.



**Open Access** This article is licensed under a Creative Commons Attribution 4.0 International License, which permits use, sharing, adaptation, distribution and reproduction in any medium or format, as long as you give appropriate credit to the original author(s) and the source, provide a link to the Creative Commons license, and indicate if changes were made. The images or other third party material in this article are included in the article's Creative Commons license, unless indicated otherwise in a credit line to the material. If material is not included in the article's Creative Commons license and your intended use is not permitted by statutory regulation or exceeds the permitted use, you will need to obtain permission directly from the copyright holder. To view a copy of this license, visit <http://creativecommons.org/licenses/by/4.0/>.

© The Author(s) 2022